AGU PUBLICATIONS

JGR

Journal of Geophysical Research: Space Physics

RESEARCH ARTICLE
10.1002/2014JA020251

Key Points:
- Cold-dense plasma is characteristically different at different locations
- Cold-dense plasma created by K-H and reconnection has lower entropy
- Interchange motion can transport cold-dense low-entropy plasma inward from flank

Correspondence to:
C.-P. Wang,
cat@atmos.ucla.edu

Citation:
Wang, C.-P., M. Gkioulidou, L. R. Lyons, X. Xing, and R. A. Wolf (2014), Interchange motion as a transport mechanism for formation of cold-dense plasma sheet, *J. Geophys. Res. Space Physics*, *119*, doi:10.1002/2014JA020251.

Received 2 JUN 2014
Accepted 29 SEP 2014
Accepted article online 2 OCT 2014

Interchange motion as a transport mechanism for formation of cold-dense plasma sheet

Chih-Ping Wang[1], Matina Gkioulidou[2], Larry R. Lyons[1], Xiaoyan Xing[1], and Richard A. Wolf[3]

[1]Department of Atmospheric and Oceanic Sciences, University of California, Los Angeles, California, USA, [2]The Johns Hopkins University Applied Physics Laboratory, Laurel, Maryland, USA, [3]Department of Physics and Astronomy, Rice University, Houston, Texas, USA

Abstract To evaluate whether interchange motion can provide the transport for the formation of the cold-dense plasma sheet in the near-Earth region, we present an event of cold-dense plasma sheet observed by five THEMIS probes after the interplanetary magnetic field turned northward, as well as their comparisons with the simulation results from the Rice Convection Model (RCM) combined with a modified Dungey force-balanced magnetic field solver. The observations of cold-dense plasma at different locations show quite different characteristics: (1) closer to the flank, the appearance is more periodic and exhibits larger fluctuations in plasma moments and magnetic field; (2) further away from the flank, the cold plasma appears later; (3) in the mixture with the cold plasma, the decrease in high-energy particle fluxes becomes less significant further away from the flank; (4) there is energy-dispersion in the cold particles at some locations; and (5) near the magnetopause, the fluctuations have the characteristics of the Kelvin-Helmholtz (K-H) vortices and the colder-denser plasma is likely to have lower entropy. In the RCM simulations, lower entropy plasma consisting of colder-denser ions and electrons was periodically released locally at the outer boundary to represent the plasma created within a K-H vortex. This lower entropy perturbation is interchange unstable and the resulting interchange motion through the magnetosphere-ionosphere coupling pushes the colder-denser plasma radially inward. The simulated particle energy spectrums at different locations qualitatively reproduce the observations, strongly suggesting that the seemingly different characteristics of cold-dense plasma observed by different probes are all a result of the same interchange-related transport mechanism.

1. Introduction

One of the most significant differences seen in the plasma sheet between northward and southward interplanetary magnetic field (IMF) periods is that the plasma sheet is colder and denser during northward IMF [e.g., *Terasawa et al.*, 1997]. The cold-dense plasma sheet state, as a precondition, has fundamental effects on the ring current intensification [*Thomsen et al.*, 2003; *Lavraud et al.*, 2006; *Chen et al.*, 2007] and magnetosphere-ionosphere coupling [e.g., *Gkioulidou et al.*, 2009] during geomagnetic storms. However, the underlying processes responsible for the formation of cold-dense plasma sheet, especially transport mechanisms, have not been fully determined.

Observations showed that a cold-dense plasma sheet forms rather gradually following the IMF becoming northward [*Terasawa et al.*, 1997; *Wing et al.*, 2005; *Wang et al.*, 2010]. The cold-dense plasma is contributed by an increase in the numbers of particles at energy lower than the thermal plasma sheet population ($>$ ~5 keV for ions and $>$ ~1 keV for electrons). The flanks are believed to be the major source locations for these low-energy particles. This flank source is likely created by magnetosheath particles that enter the magnetosphere by either directly crossing the magnetopause through processes such as Kelvin-Helmholtz instability [e.g., *Fujimoto and Terasawa*, 1994; *Otto and Nykyri*, 2003; *Nakamura et al.*, 2013], diffusion [*Johnson and Cheng*, 1997], or impulsive penetration [e.g., *Echim and Lemaire*, 2002], or through high-latitude reconnection [e.g., *Song and Russell*, 1992; *Li et al.*, 2008]. All the above mechanisms predict the flank sources to be stronger for northward than southward IMF, suggesting that a change in the flank source plays an important role in the formation of cold-dense plasma sheet.

The cold-dense plasma sheet has been observed to extend from the flanks deep into the magnetosphere [*Terasawa et al.*, 1997; *Fujimoto et al.*, 2002; *Wang et al.*, 2010], indicating that there are transport processes moving the cold particles inward. The transport is not likely provided by large-scale drift. Analysis of transport

paths shows that large-scale electric drift delivers particles earthward and outward toward the flanks, and thus cannot bring the flank source particles inward [*Wang et al*., 2007, 2009]. There are some particles from the dawn flank that can move into the midnight plasma sheet due to magnetic drift [*Spence and Kivelson*, 1993; *Wang et al*., 2004]; however, that magnetic drift is too small compared with earthward electric drift to move cold particles into the plasma sheet from the dawn flank. In addition, magnetic drift, being directed duskward, cannot transport cold ions from the dusk flank toward midnight. It has been proposed [e.g., *Borovsky et al*., 1997; *Terasawa et al*., 1997; *Borovsky and Funsten*, 2003; *Weygand et al*., 2005; *Antonova*, 2006] that diffusion due to flow turbulence may transport cold particles inward. *Wang et al*. [2010] estimated diffusion coefficients associated with turbulent flows from Geotail observations. They performed a simulation that shows that diffusive transport due to turbulence in the tail plasma sheet (r ~20–30 R_E) can move cold particles from the flank to the midnight meridian to form cold-dense plasma sheet with density increase rates consistent with the statistical Geotail results. However, the mechanisms that create the turbulent flows during northward IMF have not yet been determined.

Despite the importance of diffusion on cold-dense plasma sheet formation in the tail, the flow turbulence and the associated diffusion coefficients are much smaller in the near-Earth region ($r <$ ~15 R_E) [*Stepanova et al*., 2011] and thus may not be able to account for the near-Earth cold-dense plasma sheet. It has been suggested that the cold-dense plasma created by the reconnection within a rolled-up K-H vortex should have relatively lower entropy (entropy in this paper refers to the entropy parameter, $PV^{5/3}$, where P is plasma pressure and V is flux tube volume per unit magnetic flux) than the surrounding hot plasma sheet plasma, which can lead to interchange instability that transports the cold-dense plasma inward [*Johnson and Wing*, 2009]. Results from global MHD simulations have shown finger-like cold-dense plasma extending inward from the flanks likely driven by the K-H vortices [*Lyon*, 2011]. By including quasi-periodic entropy perturbations just inside the flank magnetopause in MHD simulations, *Otto* [2009] showed that azimuthal transport through interchange motion can carry cold-dense low-entropy plasma inward from the flanks. Interchange motion has long been considered as one major mechanism for transporting hot tenuous low-entropy plasma earthward from the tail [*Pontius and Wolf*, 1990; *Chen and Wolf*, 1993] observed during disturbed time. However, no further simulation and observational studies have been conducted to investigate the role of the interchange motion in the formation of cold-dense plasma sheet during northward IMF.

In this study we use observations and simulations to evaluate the importance of the interchange motion in the inward transportation of cold-dense plasma. In section 2, we present an event with cold-dense plasma sheet being observed by all five THEMIS probes in the near-Earth region. The observations show that characteristics of the cold-dense plasma are quite different at different locations. We then conducted simulations using the Rice Convection Model (RCM) with the particle boundary conditions changing based on the THEMIS observations. The model descriptions and the simulation results are presented in section 3. The qualitative agreement between the simulations and the THEMIS observations suggests that transport due to interchange motion plays an important role in the formation of cold-dense plasma sheet in the near-Earth region.

2. An Event Observed by Five THEMIS Probes

In this section, we describe a cold-dense plasma sheet event observed by all five THEMIS probes on 5 December 2008. The THEMIS mission consists of five probes (TH-A, TH-B, TH-C, TH-D, and TH-E) moving in low-latitude orbits. The three inner probes (TH-A, TH-D, and TH-E) cover regions inside r ~12 R_E, while the two outer probes (TH-B and TH-C) cover regions inside r ~30 R_E. The three inner probes were close to each other with a 1–2 R_E separation. Ions and electrons are measured by an electrostatic analyzer (ESA, 0.006–20 keV/q for ions and 0.007–26 keV for electrons [*McFadden et al*., 2008]) and a solid state telescope (SST, 35 keV–6 MeV for ions and 30 keV–6 MeV for electrons). For each measured energy spectrum, the penetrating radiation contamination to ESA and sunlight contamination to SST are removed (see *Wang et al*. [2011] for details).

As shown in Figure 1a, the IMF turned northward at ~18:00 UT and became strongly northward (IMF $B_z >$5 nT). The solar wind parameters were relatively steady during this northward IMF period (N_{sw} ~5.5 cm^{-3}, V_{sw} ~410 km/s, and the solar wind dynamic pressure P_{sw} ~2 nPa (P_{sw} not shown)). Geomagnetic activity became low after the IMF northward turning (*AE* decreased from 200 to 25 nT and *Dst* ~ −10 nT (*Dst* not shown)).

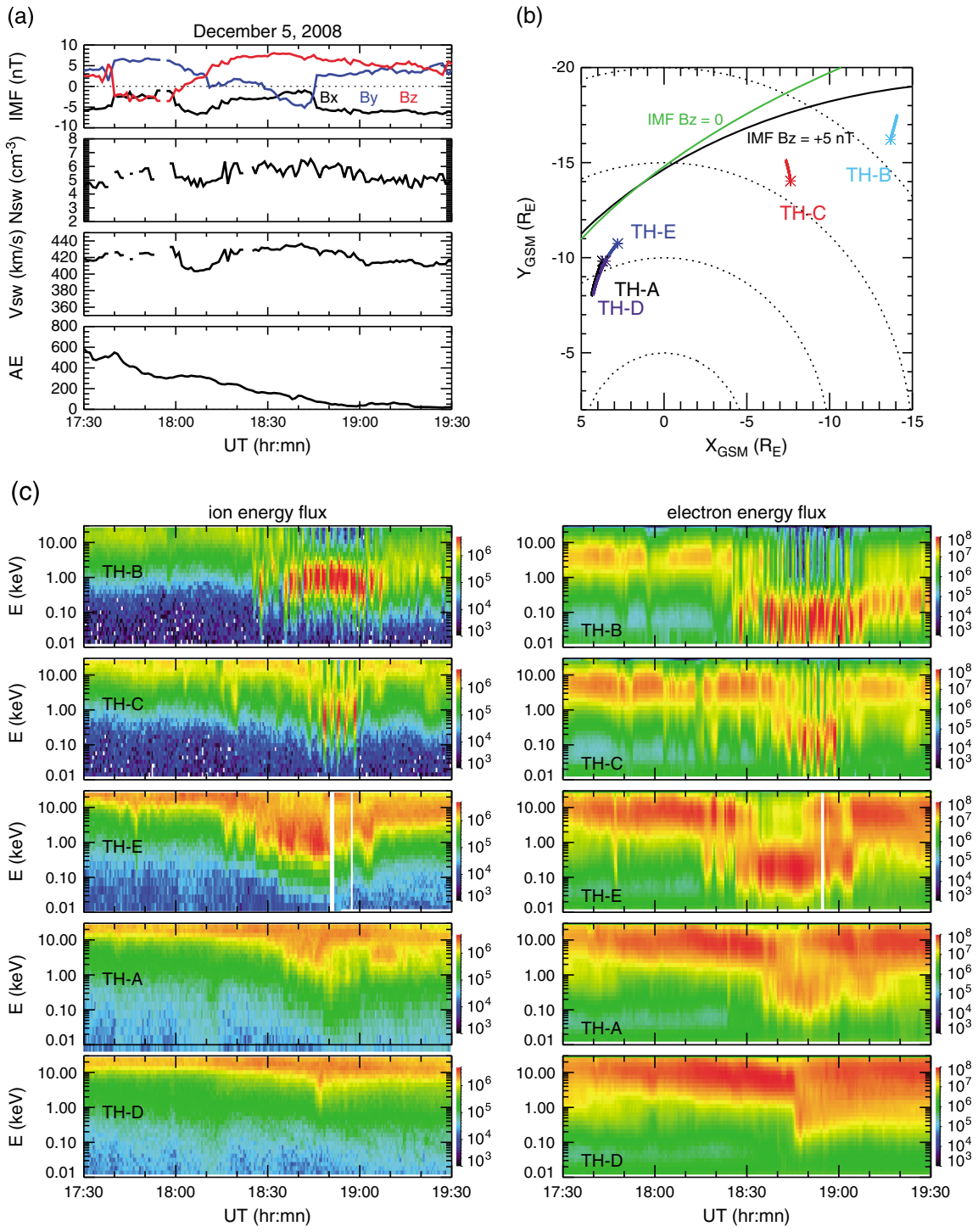

Figure 1. (a) IMF, solar wind density (N_{SW}), solar wind velocity (V_{SW}) time shifted to the Earth's bow shock, and *AE* for the 5 December 2008 event. (b) The *X-Y* projections of the trajectories for the five THEMIS probes (the asterisks indicate the probe locations at 17:30 UT). The magnetopause locations predicted by the Roelof and Sibeck model for the solar wind dynamic pressure = 2 nPa and IMF B_z = 0 (the solid green curve) and 5 nT (the solid black curves). (c) Energy spectrums of ion (left column) and electron (right column) energy fluxes (eV/(s sr cm^2 eV)) for the five THEMIS probes.

Figure 1b shows that all the five THEMIS probes were on the dawnside of the near-Earth magnetosphere with the three inner probes on the dayside at $X \sim 4$ and $Y \sim -10$ R_E (TH-A and TH-D were very close to each other in *X-Y* but were separated ~1 R_E in *Z*), TH-C on the nightside at $X \sim -8$ and $Y \sim -15$ R_E, and TH-B at $X \sim -14$ and $Y \sim -17$ R_E. All probes were a couple of Earth radii from the model magnetopause predicted using the Roelof and Sibeck model [*Roelof and Sibeck*, 1993]. The model is controlled by both P_{sw} and IMF B_z, and it predicts that the nightside magnetopause moves inward to smaller $|Y|$ as the IMF B_z increases from 0 to +5 nT and the inward displacement is larger at larger downtail distance. The three inner probes were moving away from the magnetopause, while the two outer probes were moving toward the magnetopause.

Figure 1c shows the ion and electron energy spectrums for the five probes. Before 18 UT, the peak energy is above 10 keV for the main ion population and is above 1 keV for electrons. These are typical thermal energies for hot plasma sheet populations in the near-Earth magnetosphere [*Wang et al*., 2011]. After the IMF became northward, all five probes observed cold-dense plasma as indicated by the clear increase in the particle energy fluxes at lower energy (ions from ~1 to 10 keV and electrons from ~0.1 to 1 keV). Different probes observed the cold-dense plasma at different time. For the inner probes, it was first observed by TH-E at ~1815 UT, later by TH-A at ~1830 UT, and then by TH-D at ~1845 UT. For the outer probes, TH-B started to observe cold-dense plasma at ~1825 UT and TH-C observed it at ~1842 UT. There are also differences in the characteristics of the cold-dense plasma appearance in terms of its fluctuations, mixing with the hot plasma sheet, and energy dispersion. The appearance of cold particles is more clearly periodic (~1 to 2 min) and with larger fluctuations as seen at TH-B and TH-C than at TH-E and TH-A locations, while no clear fluctuations were observed by TH-D. For TH-C before 18:35 UT and TH-E before 18:27 UT, the cold-dense plasma appearance is more transient. At ~1840 UT, TH-B encountered the magnetopause (likely due to the magnetopause moving inward in response to the IMF B_z becoming more positive) and moved in and out of the magnetosheath periodically from ~1840 to 1855 (as indicated by the disappearance of hot plasma sheet particles and strong tailward bulk flow as shown later in Figures 2 and 3) with a period similar to the fluctuations observed at other probes. As discussed later, the periodic fluctuations observed by TH-B are likely due to the K-H vortices. The mixing of the cold and hot particles is different at different probes. For both ions and electrons at the TH-B, TH-C, and TH-E locations, the fluxes of hot particles decreased significantly when those of cold particles were enhanced. But for ions and electrons at the TH-A and TH-D locations, the fluxes of hot particles remain when mixing with cold particles. The appearance of cold particles can be energy dispersive. TH-A saw an increase in 5 keV ion fluxes earlier than the increase in 1 keV ions, while there is only a weak dispersion signature in the electron fluxes at ~0.1 keV. On the other hand, the increase of cold ions and electrons is dispersionless at the TH-D location.

Figure 2 shows the changes in ion density and temperature, magnetic field, and ion perpendicular bulk velocities associated with the cold-dense plasma sheet observed by different THEMIS probes. Like the energy fluxes shown in Figure 1c, these changes appear more periodic and with stronger fluctuations at TH-B and TH-C than at other locations. However, clear fluctuations in the bulk flows can still be seen at TH-A and TH-D despite the changes in other parameters being rather smooth. Figure 3 shows more details of the fluctuations observed by TH-B and TH-C. TH-B was in the vicinity of the magnetopause as indicated by its excursion into the magnetosheath from ~1840 to 1855 UT (high density and strong tailward). The fluctuations, with a period of ~1–2 min, have characteristics similar to those previously observed by Geotail [*Fairfield et al*., 2000] and THEMIS [*Nakamura et al*., 2013] at the magnetopause that have been shown to be consistent with the fluctuations caused by the K-H vortices predicted by MHD [*Otto and Fairfield*, 2000] and particle-in-cell simulations [*Nakamura et al*., 2013]. Typically, as satellite moves from the magnetosphere to the magnetosheath, tailward V_x is expected to increase with increasing density. However, Figure 3b shows that sometimes higher-density plasma can have weak tailward V_x (for example, $|V_x| < 50$ km/s for $N \sim 4$ cm^{-3}), or lower density plasma have strong tailward flow (for example, $|V_x| \sim 200$ km/s for $N < 0.5$ cm^{-3}). This indicates that a fraction of lower density magnetospheric plasma (higher-density magnetosheath plasma) is moving with speed higher (lower) than that of the magnetosheath flow, which has been shown to result from rolled-up K-H vortices [*Takagi et al*., 2006; *Hasegawa et al*., 2006]. Figure 3c shows that the fluctuations seen at TH-C also have a period of 1 to 2 min. The decrease of hot plasma sheet particles and increase of tailward flow associated with the cold-plasma appearance are much smaller than those of the magnetosheath plasma seen at TH-B, indicating that TH-C was likely inside the magnetosphere. Similar to Figure 3b, the V_x-*N* correlations shown in Figure 3d suggest that the fluctuations are associated with the K-H vortices. The increase

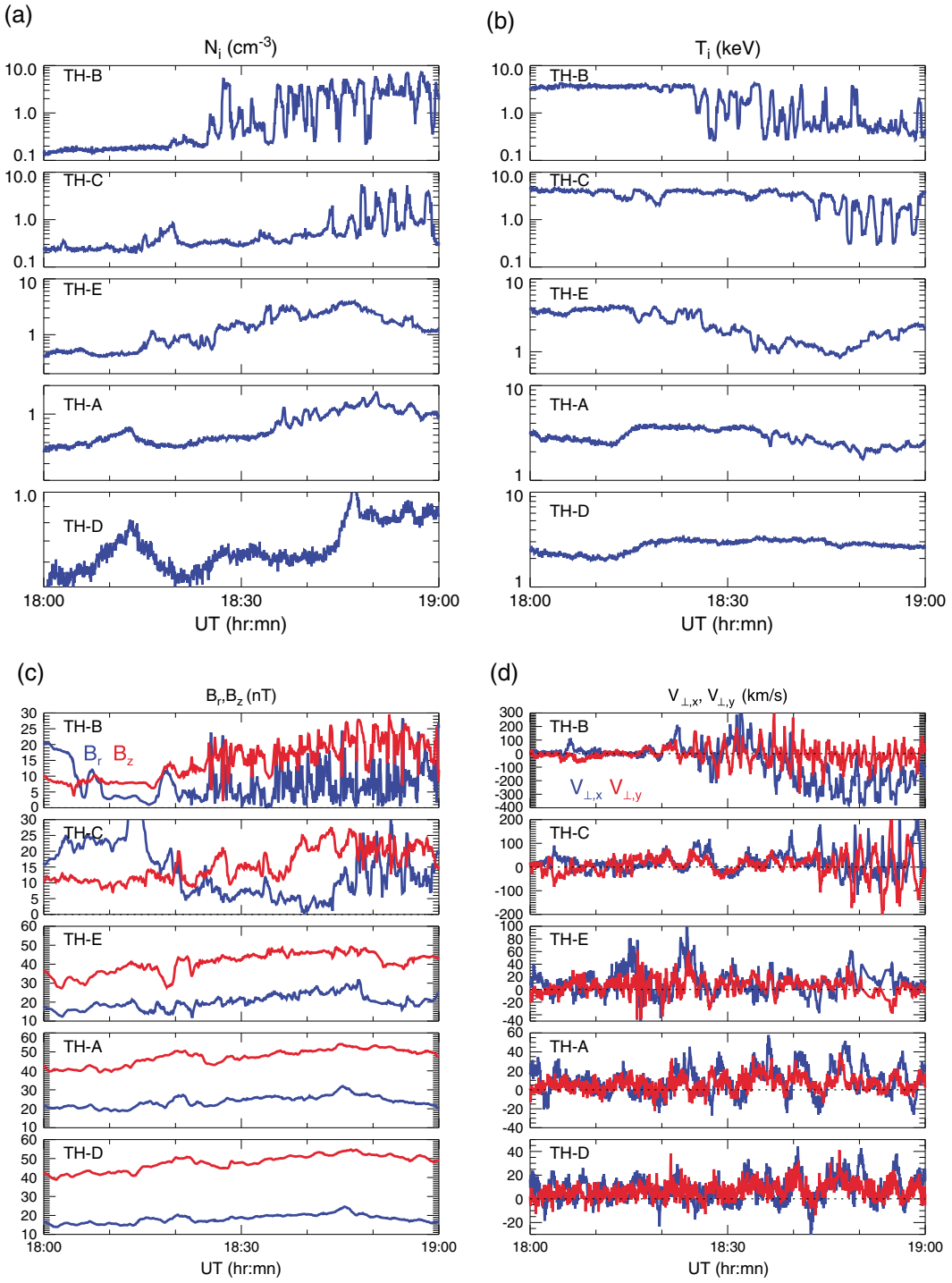

Figure 2. (a) Ion number density, (b) ion temperature, (c) the radial and B_z magnetic field components, and (d) the *X* and *Y* components of perpendicular ion bulk velocity for the five THEMIS probes.

of cold-particle fluxes and density at 18:43:40, 18:46:50, and 18:58:10 UT corresponds to a B_z increase and a B_r decrease, but little change in plasma pressure, while other cold-dense plasma increases correspond to large decreases in plasma pressure and large increases in B_r. We estimated the flux tube volume using the Wolf formula, which is based on a simple two-dimensional analytic model of plasma in force equilibrium [*Wolf et al.*, 2006]. It is currently the best tool available for providing reasonably good estimates of flux tube volume from

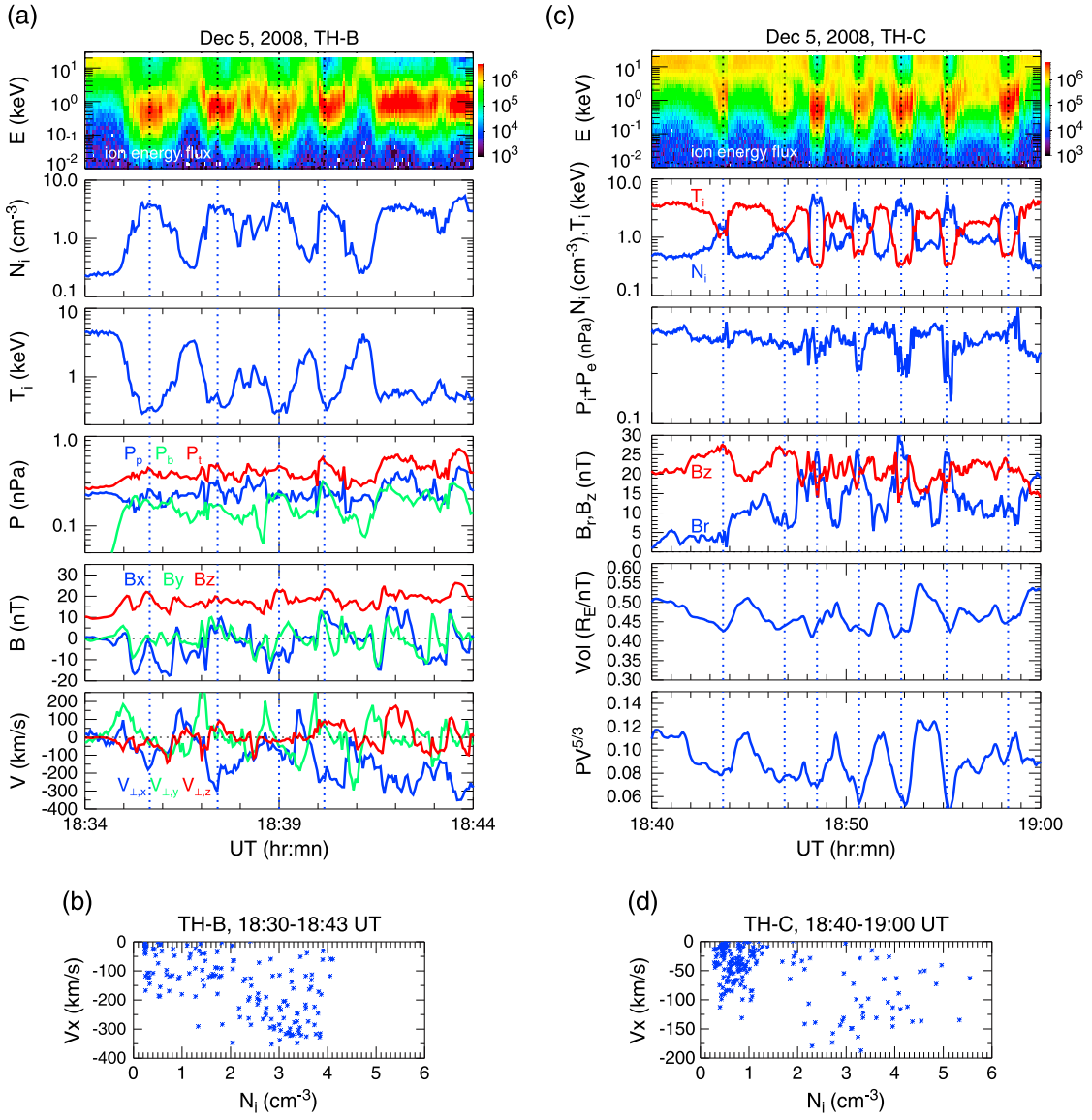

Figure 3. (a) TH-B observations of ion energy fluxes (eV/(s sr cm^2 eV)), ion density and temperature, plasma pressure (ion plus electron pressure in blue), magnetic pressure (in green), total pressure (plasma plus magnetic pressure in red), the three magnetic field components, and the three perpendicular bulk velocity components. (b) N_i-V_x correlations observed by TH-B from 18:30 to 18:4 UT. (c) TH-C observations of ion energy fluxes, ion density (blue), and temperature (red), plasma pressure, the magnetic field radial (blue) and B_z (red) components, flux tube volume, and entropy (nPa-(R_E/nT)$^{5/3}$). (d) N_i-V_x correlations observed by TH-C from 18:40 to 19:00 UT.

observations within the closed field line region. The formula has been evaluated to provide a good estimate in the plasma sheet under the conditions of slow perpendicular flow ($V_\perp \leq 150$ km/s) and $B_r/B_z \leq 3$, which are satisfied by the plasma and magnetic field observed at the TH-C location but not at the TH-B location during this period of interest. Thus, we used it to estimate the flux tube volume for the TH-C observations assuming the observed pressure and magnetic field are in equilibrium. Note that the purpose of this estimation is to investigate whether there are also fluctuations in the flux tube volume and $PV^{5/3}$ associated with the observed fluctuating pressure and magnetic field, not to obtain the exact magnitudes of these parameters. It can be seen clearly that flux tube volume and $PV^{5/3}$ decreased in association with the increase in cold particles. The smaller flux tube volume can possibly result from reconnection of field lines within the K-H vortex [*Nykyri and Otto*, 2001; *Faganello et al.*, 2012; *Ma et al.*, 2014; *Nakamura et al.*, 2013], which allows the cold-dense plasma to transfer from the magnetosheath field lines into the magnetosphere closed field

lines. This suggests that the K-H instability and subsequent reconnection allow the cold particles from the magnetosheath to enter the plasma sheet, creating cold-dense plasma with relative lower entropy than that of hot plasma sheet plasma.

The main characteristics of the cold-dense plasma revealed by this event are (1) closer to the flank, the appearance is more periodic and shows larger fluctuations in plasma moments and magnetic field; (2) further away from the flank, appearance is seen at later time; (3) in the mixture with the cold plasma, the decrease in high-energy particle fluxes becomes less significant further away from the flank; (4) there is energy dispersion in the cold particles at some locations; and (5) near the magnetopause, the fluctuations have the characteristics of the Kelvin-Helmholtz (K-H) vortices and the colder-denser plasma is likely to have lower entropy. This entropy gradient perturbation can be interchange unstable [e.g., *Xing and Wolf*, 2007]. Statistically, entropy in the near-Earth magnetosphere decreases radially inward [*Wang et al*., 2009], and interchange motion may bring the low-entropy plasma observed at the flanks inward. In the next section we used the RCM simulations to evaluate this transport by the interchange motion.

3. The RCM-Dungey Simulations

3.1. The RCM

To simulate transport of protons and electrons of different energies, we use the RCM. Here we briefly describe the working principle of our RCM simulations. The original RCM [*Harel et al*., 1981; *Toffoletto et al*., 2003] computes species- and energy-dependent particle transport and convection electric field self-consistently. The RCM is thus suitable for evaluating plasma sheet dynamics in which energy- and species-dependent processes and M-I coupling play an important role. In the ionosphere, where the induction electric field can be neglected and the grid rotates with the Earth, transport of a flux tube filled with an isotropic distribution of ions or electrons at specified kinetic energies E_k by bounce-averaged electric drift and magnetic drift can be written as [*Wolf*, 1983]

$$V_D(\mathbf{x},t) = \frac{\mathbf{B}(\mathbf{x},t)\times\nabla\Phi(\mathbf{x},t)}{|\mathbf{B}(\mathbf{x},t)|^2} + \frac{\mathbf{B}(\mathbf{x},t)\times\lambda\nabla V(\mathbf{x},t)^{-2/3}/q}{|\mathbf{B}(\mathbf{x},t)|^2}, \quad (1)$$

where Φ is electric potential and V is flux tube volume. The energy invariant is $\lambda = E_k V^{2/3}$, which is constant along a particle's drift path. Thus, as a particle moves along its drift path, its energy changes as V changes. The inertial term is neglected in the momentum equation. The model domain is inside the closed field line region. The RCM grids are specified in the ionosphere, so **B** in equation (1) is the magnetic field in the ionosphere. The grid used in this simulation is uniformly distributed in the longitudinal direction (0.5 MLT (magnetic local time) spacing) but nonuniformly distributed in the latitudinal direction (~0.5° spacing at latitudes between 55° and 75° and larger at other latitudes). A 3-D distribution of magnetic field is required for computing V and field-aligned currents (FACs, $j_{||}$), and for the mapping from the ionosphere to the magnetotail. When **B** is computed self-consistently with plasma pressure, drift due to induced electric field is included in computing motions in the magnetosphere. Note that the bulk flows measured by spacecraft in the plasma sheet, like those shown in Figures 2 and 3 include electric drift (convection plus corotation plus induced electric field), magnetic drift, and magnetization drift (due to nonuniform plasma and magnetic field). All these drifts can be computed in our simulations.

The magnetosphere and ionosphere are coupled through

$$j_{||,i} = (B_i/B_e)\left(\mathbf{b}\cdot\nabla_{eq}V\times\nabla_{eq}PV^{5/3}\right)/V^{5/3} \quad (2)$$

computed using the Vasyliunas equation [*Vasyliunas*, 1970], where subscript i (eq) refers to quantities in the ionosphere (the equatorial plane) and P is plasma pressure. To maintain current continuity in both the magnetosphere and ionosphere [*Vasyliunas*, 1970; *Wolf*, 1983], the electric field in the ionosphere changes self-consistently depending on $j_{||}$ and the height-integrated conductance Σ

$$\nabla_i\cdot[\Sigma\cdot\nabla_i\Phi_i] = -j_{||,i}\sin(I), \quad (3)$$

where I is dip angle. With given Σ and Φ_i boundary conditions at the high- and low-latitude boundaries, (3) can be solved to obtain Φ_i. The high-latitude boundary condition for the potential is a Dirichlet boundary condition; the overall strength of convection is determined by setting the total range of potential

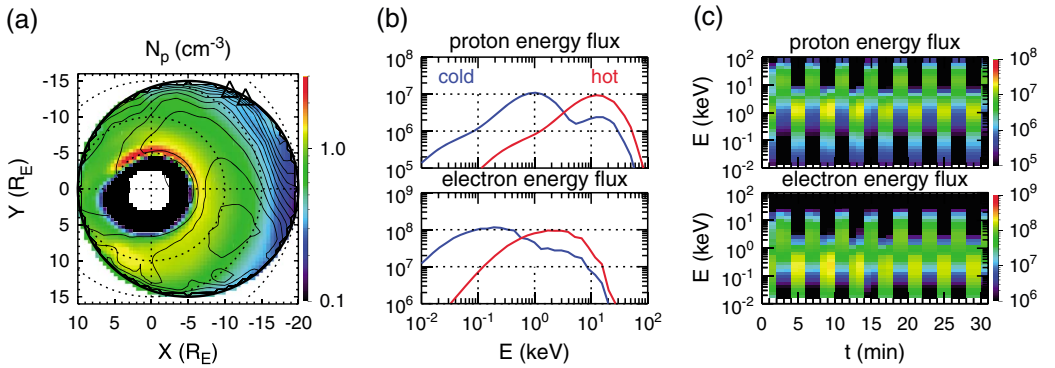

Figure 4. (a) Equatorial distribution of the RCM proton density and electric potential contours (1 kV intervals) from the initial condition. The black solid circle indicates the RCM outer boundary and the two triangles mark 3 and 3.5 MLT, respectively. (b) Proton and electron energy spectrums of energy fluxes for the hot (the red curves) and cold-dense (the blue curves) plasma boundary conditions at 3 MLT. (c) The proton and electron energy fluxes (eV/(s sr cm^2 eV)) of the cold-dense plasma boundary condition used in Run1 at 3 MLT as a function of time.

on the boundary equal to the polar cap potential (Φ_{PC}). Φ_{PC} is thus the external driver of convection. A two-cell convection pattern is assigned to describe the electric potential inside the polar cap. The low-latitude boundary condition incorporates the effects of the equatorial electrojet. The conductance includes Solar-EUV-generated conductance and the Hall and Pedersen auroral conductance computed from simulated electron precipitation. The electron precipitation is computed from the simulated particle spectrums and precipitation loss rates (in our simulation runs the field-aligned potential drop is assumed to be zero). In our simulation, the *Chen and Schulz* [2001] electron loss rate is used (see *Gkioulidou et al.* [2012] for more details).

To provide the RCM with self-consistent magnetic fields, we use a modified Dungey force-balanced magnetic field solver [*Liu et al.*, 2006; *Schulz and Chen*, 2008] to obtain magnetic fields that are in approximate force balance with the simulated plasma pressures in the equatorial plane. This allows us to achieve satisfactory force balance near the equatorial plane while retaining model flexibility (see *Gkioulidou et al.* [2011] for details).

Protons and electrons of different energies released from the RCM outer boundary move inside the model region along their electric and magnetic drift paths. The boundary particle flux distributions are modeled by dividing particles into several energy channels (currently 80 proton and 30 electron channels with energy ranges from ~10 eV to 300 keV). We have used 11 years of Geotail observations to establish the proton and electron distributions at different MLT along the RCM outer boundary (we defined the equatorial boundary location by a 15 R_E circle centered at $X = -5$ R_E and $Y = 0$, see Figure 4a) by fitting the observed spectrums with two-component kappa distributions, which are a combination of one cold and one hot population [*Wang et al.*, 2011]. Since observed plasma sheet particle distributions are not a single Maxwellian, the two-component kappa distributions better describe the number of particles at different energies.

Simulations based on the RCM have been used to study the plasma sheet structures driven by steady convection [*Wang et al.*, 2011] and by local plasma perturbations such as plasma bubbles [e.g., *Yang et al.*, 2011, 2012, 2014]. The major differences between the RCM simulations used in the current study and that used in *Yang et al.* studies (called RCM-E) include different outer boundary particle sources, electron loss rates, and magnetic field solver.

3.2. Simulation Setup

We first run the RCM simulation to establish the initial conditions for particles and fields by populating the model domain with particles coming from the outer boundary. The particle boundary conditions for the protons and electrons are identical to those used in *Wang et al.* [2011] for high Φ_{PC} (see Figure 5 of *Wang et al.* [2011] for the MLT distributions of the parameters used in specifying the boundary particle fluxes). We first ran the simulation for 8 h and 30 min under strong convection (Φ_{PC} = 90 kV), and then weakened the convection to 30 kV for another 30 min to represent the IMF becoming northward. The particle boundary conditions were kept constant for this 9 hr period. The results at the end are used as the initial conditions for the following simulations.

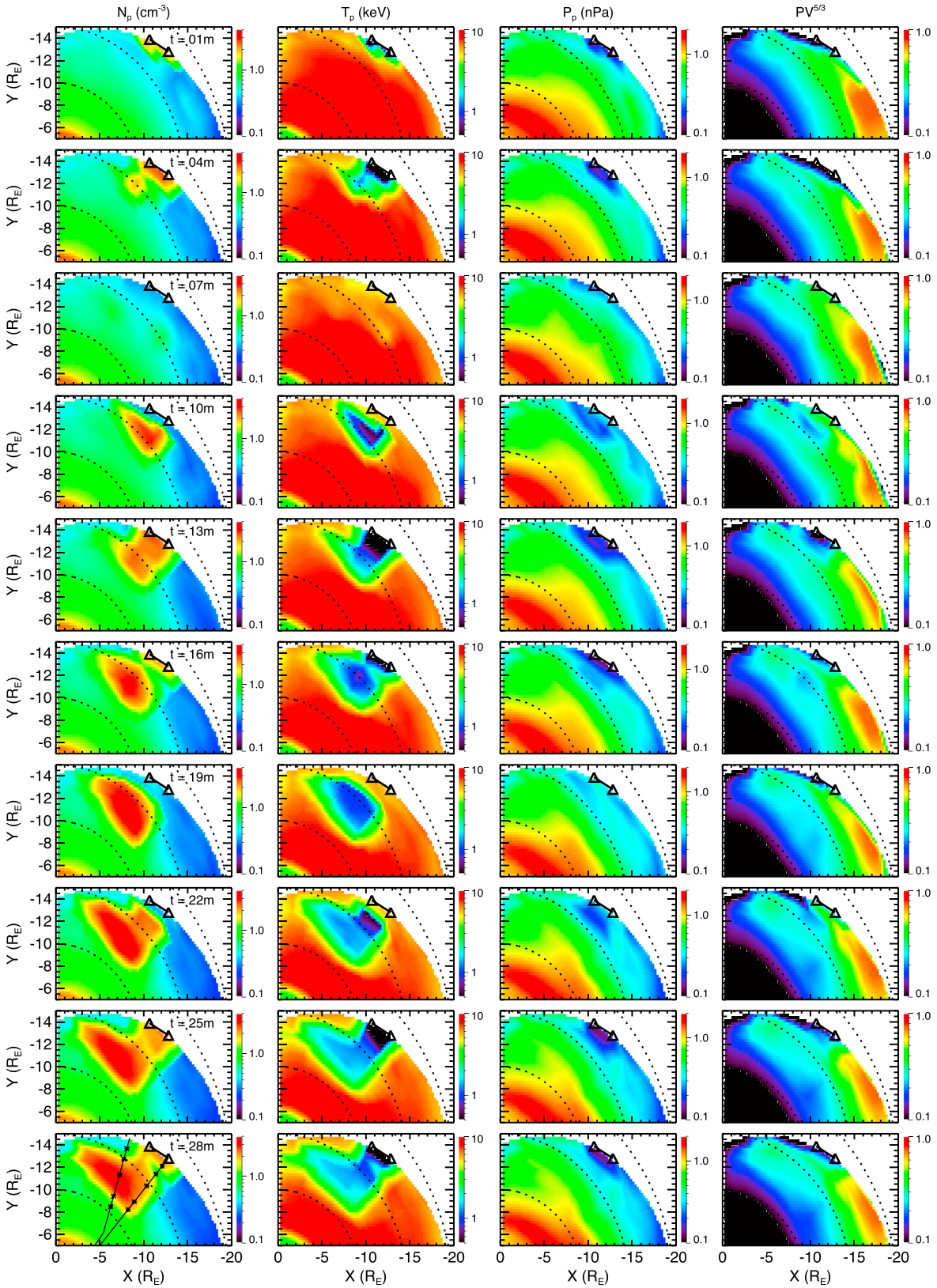

Figure 5. Equatorial distributions of the RCM proton density, proton temperature, proton pressure, and entropy at different times. The two triangles in each plot mark 3 and 3.5 MLT. The solid black lines in the N_p plot for t = 28 m are the 3 and 4 MLT radial lines, and the five dots along each line indicate the locations where temporal profiles of RCM parameters are plotted in Figures 7 and 8.

The goal of this simulation is to evaluate the evolution of cold-dense low-entropy plasma presumably created by the K-H instability and subsequent reconnection at the flank magnetopause but not to investigate these two creation processes. The RCM only simulates the closed field line region of the magnetosphere, thus cannot include the magnetosheath to simulate the K-H instability at the magnetopause. The RCM also neglects inertial currents, which play an important role in K-H instability. Therefore, in this simulation we specified outer boundary particle condition to represent the cold and dense particles that have already entered the closed field line region, and the plasma and magnetic field have come to quasi-equilibrium after the K-H and reconnection process so that their subsequent evolution can be modeled by the RCM physics. The cold-dense low-entropy plasma is specified at the outer boundary by locally and periodically changing particle fluxes based on the TH-C observations shown in Figure 3c. The MLT and temporal variations of this K-H particle boundary condition are specified as following: (1) for all MLTs except 3–3.5 MLT, boundary particle fluxes are the same as those used in establishing the initial conditions described above (we refer this as "hot plasma" condition) and are kept time independent. (2) At 3–3.5 MLT (as marked by the two triangles in Figure 4a), the conditions are switched between hot and cold-dense plasma every 2 min (that is, cold-dense plasma at t = 1–2, 5–6, 9–10, … and hot plasma at t = 3–4, 7–8, 11–12, …). For the cold-dense plasma, the proton and electron temperatures (for both the hot and cold components of the two-component kappa distribution) are a factor of 12 lower and densities (also for both components) are a factor of 6 higher than those of the hot plasma (so plasma pressures and entropy are a factor of 2 lower). These magnitude changes are similar to those observed by TH-C. The particle fluxes for the hot and cold-dense plasma at 3 MLT are shown in Figure 4b. The energy spectrums as a function of time at 3 MLT are shown in Figure 4c. We conducted two simulation runs: (Run1) with the K-H boundary condition, we ran the simulation from t = 0 to 30 min under constant Φ_{PC} = 30 kV. (Run2) the simulation was run with time-independent hot plasma condition for all MLT. In Run2, the plasma and fields gradually approached a steady state, providing undisturbed magnetosphere state for comparison. When the cold-dense low-entropy plasma boundary condition is switched on and off, we keep the high-latitude electric potential boundary condition (the potential at the open-closed field line boundary) to be constant. In both simulation runs, electric field is updated every 2 s and magnetic field is updated every minute.

3.3. Evolution of Cold-Dense Low-Entropy Plasma

Figure 5 shows evolution of simulated proton density, temperature, pressure, and entropy in the equatorial plane from Run1, while ionospheric FACs (mapped to the equator), electric potential, and proton bulk velocities are shown in Figure 6. It can be seen that cold-dense plasma from 3 to 3.5 MLT moves ~7 R_E radially inward into the magnetosphere in 30 min. The deepest penetration is along the 3 MLT radial line (as indicated by the solid black line further to the right in the density plot for t = 28 m). In addition, the cold-dense plasma also moves toward dawn. The cold-dense plasma has relatively lower pressure and entropy than its surrounding plasma near the boundary as imposed by the boundary condition, but the differences become smaller as the cold plasma penetrates deeper radially. Also, there is no clear entropy difference caused by the cold plasma that is moving dawnward. The perturbations in FACs caused by the cold plasma associated entropy gradient are mostly near the 3–3.5 MLT boundary and near the 3 MLT line. In response to this rather azimuthally localized FAC perturbation, changes in the electric potential distribution are seen over much wider MLT and radial distance ranges. As a result, bulk flows with changes in both directions and magnitudes occur over a wide region both within and outside the cold-dense plasma.

To show more clearly the perturbations in the magnetosphere caused by the cold-dense low-entropy plasma released at the boundary, we plot in Figure 7 the temporal variations of different parameters from both Run1 (the red lines) and Run2 (the blue lines) at five different radial distances away from the boundary (dR) along the 3 MLT line as indicated by the dots shown in the density distribution for t = 28 min in Figure 5. For Run1, the cold and dense plasma gradually reaches deeper into the magnetosphere. While the changes in plasma moments are periodic near the boundary, reflecting the imposed K-H boundary condition, the changes become smoother further away except for the bulk velocities. The periodic fluctuations at the same location are larger at the beginning and become smaller later. In comparison, without the cold low-entropy plasma from the boundary in Run2, no large fluctuations are seen as the magnetosphere gradually reaches an equilibrium steady state.

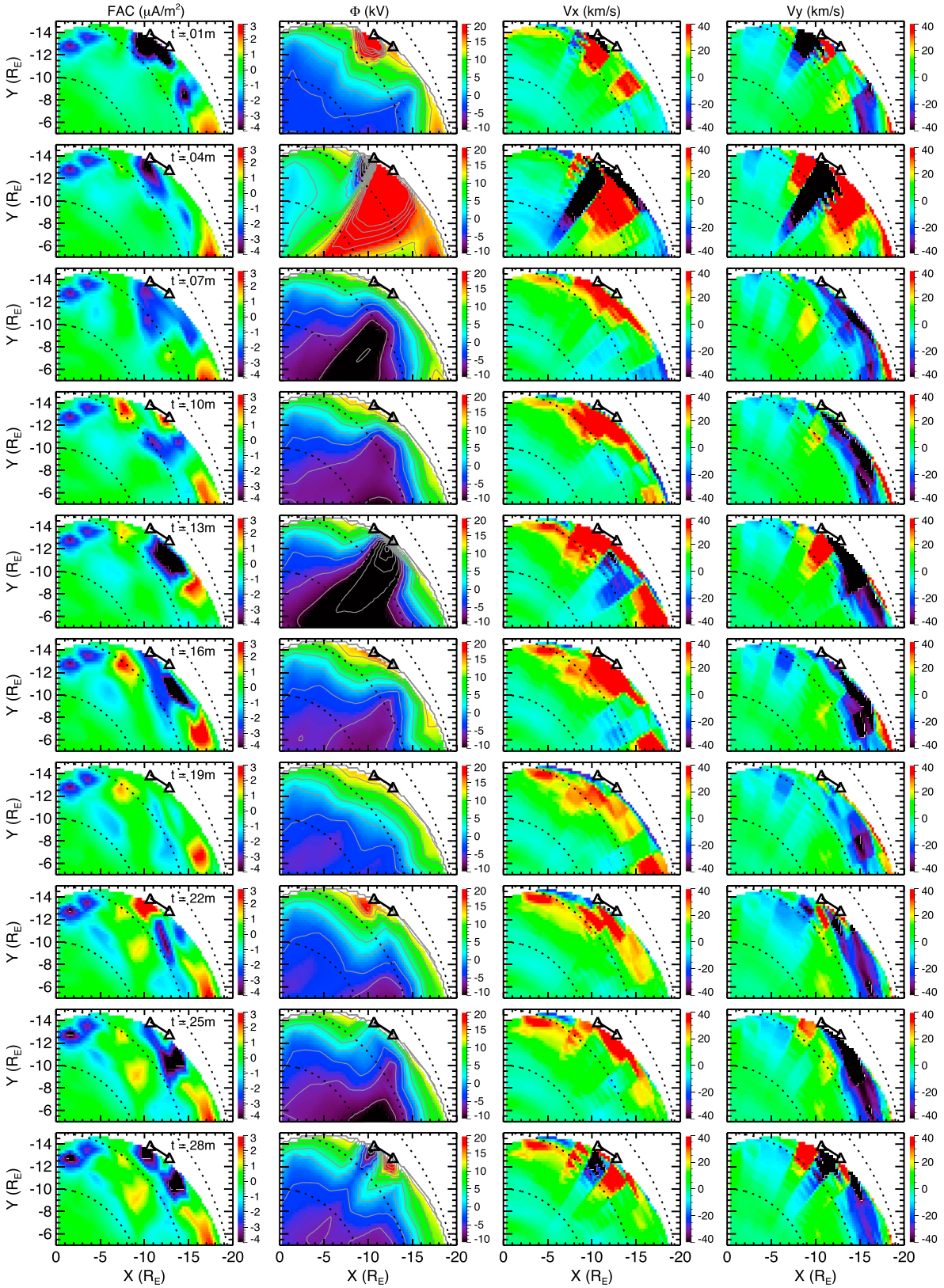

Figure 6. Equatorial distributions of the RCM ionospheric FACs mapped to the equator (positive (negative) FAC indicates current flowing into (from) the ionosphere), electric potential and contours (with 3 kV intervals), proton perpendicular bulk velocities in the *X* and *Y* directions for different times. The two triangles in each plot mark 3 and 3.5 MLT.

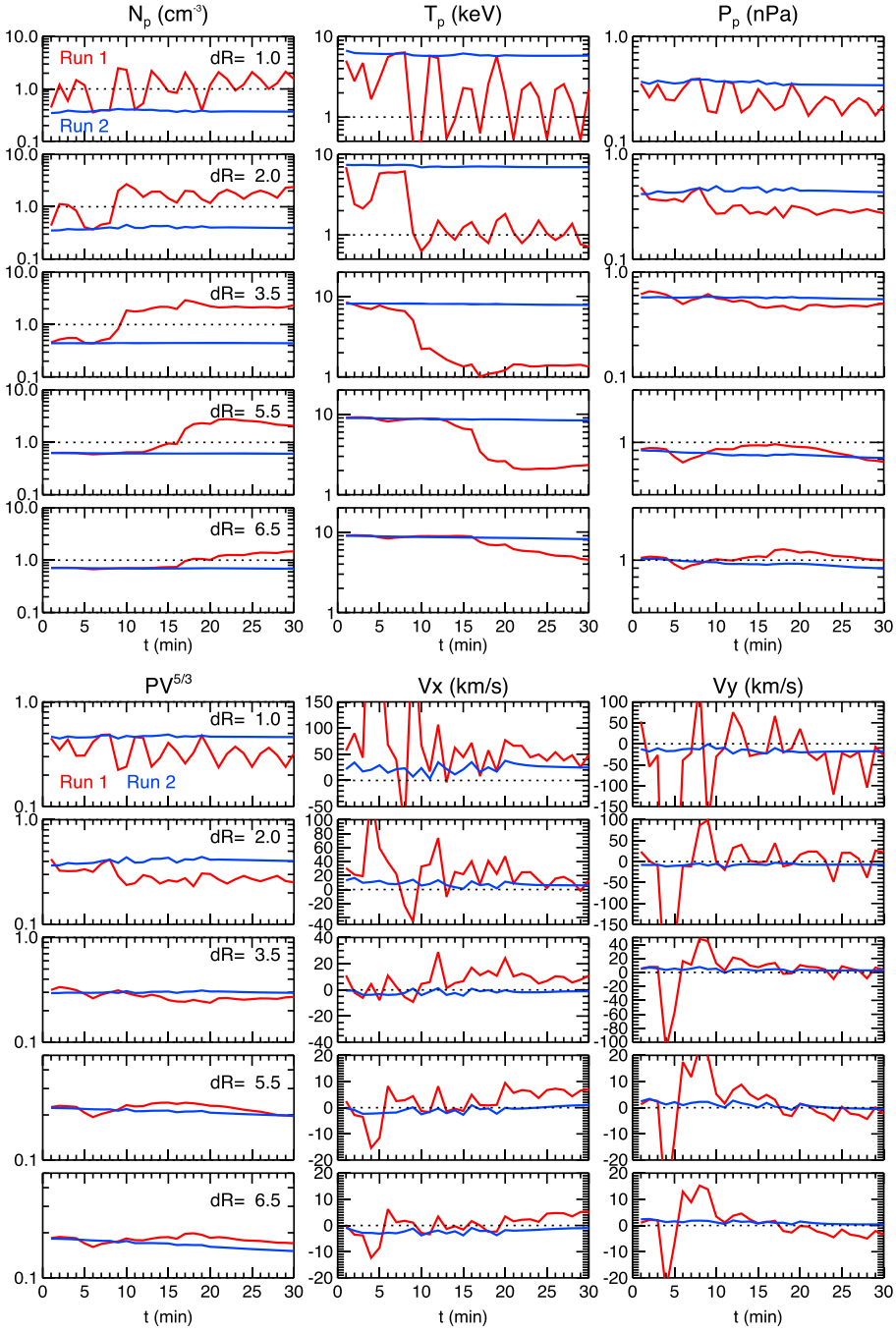

Figure 7. Temporal variations of the RCM proton density, temperature, pressure, entropy, and proton perpendicular bulk velocities in the *X* and *Y* directions from Run1 (the red lines) and Run2 (the blue lines) at the five locations along the 3 MLT radial line indicated by the black dots in the N_p plot for t = 28 m shown in Figure 5.

Figures 8a and 8b show the temporal variations of proton and electron energy fluxes along the 3 and 4 MLT lines, respectively. Along the 3 MLT line, low-energy particles reach deeper into the magnetosphere at later time (~17 min to reach $dR = 6.5\ R_E$), but different characteristics are seen at different locations. The appearance of cold plasma is more periodic near the boundary as seen at $dR = 1$ and 2 R_E, which is similar to those observed by TH-B and TH-C, but becomes smoother deeper inside the magnetosphere, like those seen by TH-A and TH-D. At $dR \leq 3.5\ R_E$, the cold-dense plasma at $t < 9$ min appears transiently, similar to the transient features seen at TH-C before 1835 UT and TH-E before 1827 UT. The appearance can be gradual and

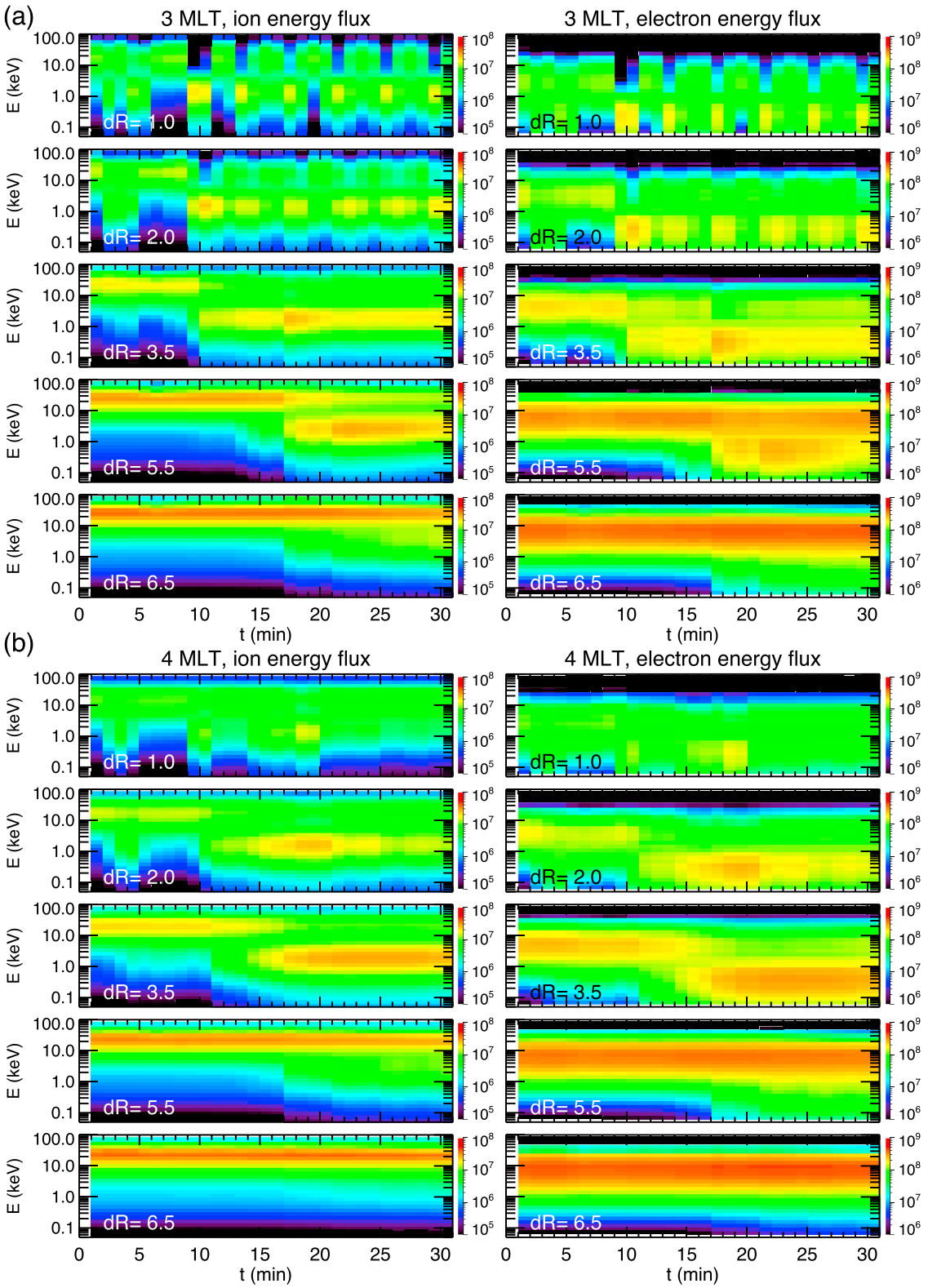

Figure 8. Temporal variations of the RCM proton and electron energy fluxes (eV/(s sr cm^2 eV)), the five locations along the (a) 3 MLT and (b) 4 MLT radial line are indicated by the black dots in the N_p plot for t = 28 m shown in Figure 5.

with energy dispersion (lower energy ions appears later) as seen at dR = 3.5 and 4.5 R_E and at TH-E and TH-A locations, or can be sharp and dispersionless as seen at dR = 6.5 R_E and at TH-D location. In addition, there are different degrees of mixing with hot plasma. Closer to the boundary, fluxes for high-energy particles decrease significantly when cold particles appear, as seen at dR = 1 and 2 R_E and at TH-B and TH-C locations. But the decrease becomes smaller at larger dR, similar to what was observed at TH-E, TH-A, and TH-D (TH-A and TH-D were further away from the model magnetopause than was TH-E as shown in Figure 1b). Along the 4 MLT line, no periodic fluctuations are seen at all dR. At larger dR, cold-dense plasma appears later than it does at 3 MLT, indicating the cold plasma moves inward first and then moves azimuthally dawnward. The above qualitative consistencies between simulations and observations strongly suggest that the seemingly different characteristics of the cold-dense plasma observed by different THEMIS probes can result from the same interchange motion associated with one or more K-H vortices. This will be further discussed in section 4.

3.4. Interchange Motion

In this section we describe the magnetosphere-ionosphere coupling process leading to the interchange motion that transports cold-dense low-entropy plasma inward into the magnetosphere. Figure 9a shows entropy, ionospheric FACs and Pedersen conductance mapped to the equatorial plane, proton number density together with electric potential contours and the E × B directions, and energy fluxes and total drift (electric plus magnetic drift but not magnetization drift) paths and directions for 1 and 20 keV protons from Run1 at t = 13 min when the cold-dense boundary condition is switched on. The undisturbed magnetosphere from Run2 is also shown in Figure 9b for comparison. When the colder-denser lower entropy plasma is imposed at the boundary locally, it results in large changes in the entropy gradients ($\nabla PV^{5/3}$, as indicated by the blue vectors) surrounding the colder-denser plasma. $\nabla PV^{5/3}$ becomes significantly diverted from the gradients of flux tube volume (∇V, as indicated by the red vectors), thus a new pair of FACs forms with upward (downward) FACs near the westward (eastward) edge of the colder plasma according to equation (2). The smaller number of high-energy electrons in the colder plasma produces smaller energy fluxes of precipitating electrons and thus lower ionospheric conductance [e.g., *Robinson et al.*, 1987]. To determine if this lower entropy plasma is susceptible to interchange instability, we computed the growth rate against long wavelength perturbation, rate $\propto -\cos\alpha + \beta R/(2(1 + 5/6\beta))$ [*Xing*, 2008], where α is the angle between $\nabla PV^{5/3}$ and ∇V, $R = (V/PV^{5/3})|\delta(PV^{5/3})/\delta V|$, and β is the plasma beta averaged over the entire flux tube. It can be seen that $\nabla PV^{5/3}$ and ∇V are almost antiparallel at the inward edge of the lower entropy plasma, which gives positive $\cos\alpha$. The computed growth rates are also plotted with line contours. The growth rate is <0 (indicated by the black contours) in most of the plasma sheet region but is >1 (indicated by the white contours) in the region of the lower entropy plasma, indicating it is indeed interchange unstable. In comparison, the plasma sheet in Run2 is interchange stable.

In response to these perturbations in FACs and conductance, the spatial distribution of the electric potential is changed to maintain current continuity in the ionosphere according to equation (3). The perturbed FAC flows into (out of) the ionosphere at the eastward (westward) edge of the colder plasma, thus giving rise to westward current flowing in the ionosphere for the current closure. As a result, the electric field within the lower entropy plasma becomes westward and enhanced with the E × B drift pointed radially inward, pushing particles in this lower entropy plasma deeper into the magnetosphere as indicated by their drift paths. The enhancement is partly contributed by the lower conductance since to provide the same ionospheric current, electric field is larger when conductance is lower. The electric field outside the lower entropy plasma is also changed with an enhancement in the E × B drift near the westward edge pointed toward eastward, moving particles azimuthally from the surrounding higher-entropy plasma to replace the lower entropy plasma. Despite that the higher entropy in the surrounding plasma is contributed by higher energy ions whose drift becomes more affected by westward magnetic drift when energy is higher, the enhanced westward electric drift is able to divert some of the high-energy ions (those of relatively lower energy thus weaker magnetic drift) into the lower entropy region. This is the interchange motion that works to diminish the entropy gradient perturbation introduced by the lower entropy plasma. Through this interchange motion, a large number of cold particles within the lower entropy plasma are transported inward in the magnetosphere to form the cold-dense plasma sheet.

The perturbed electric drift moves plasma eastward of the 3 MLT line inward, while it moves plasma westward of the 3 MLT line outward to complete the interchange motion. The electric drift perturbations are largest

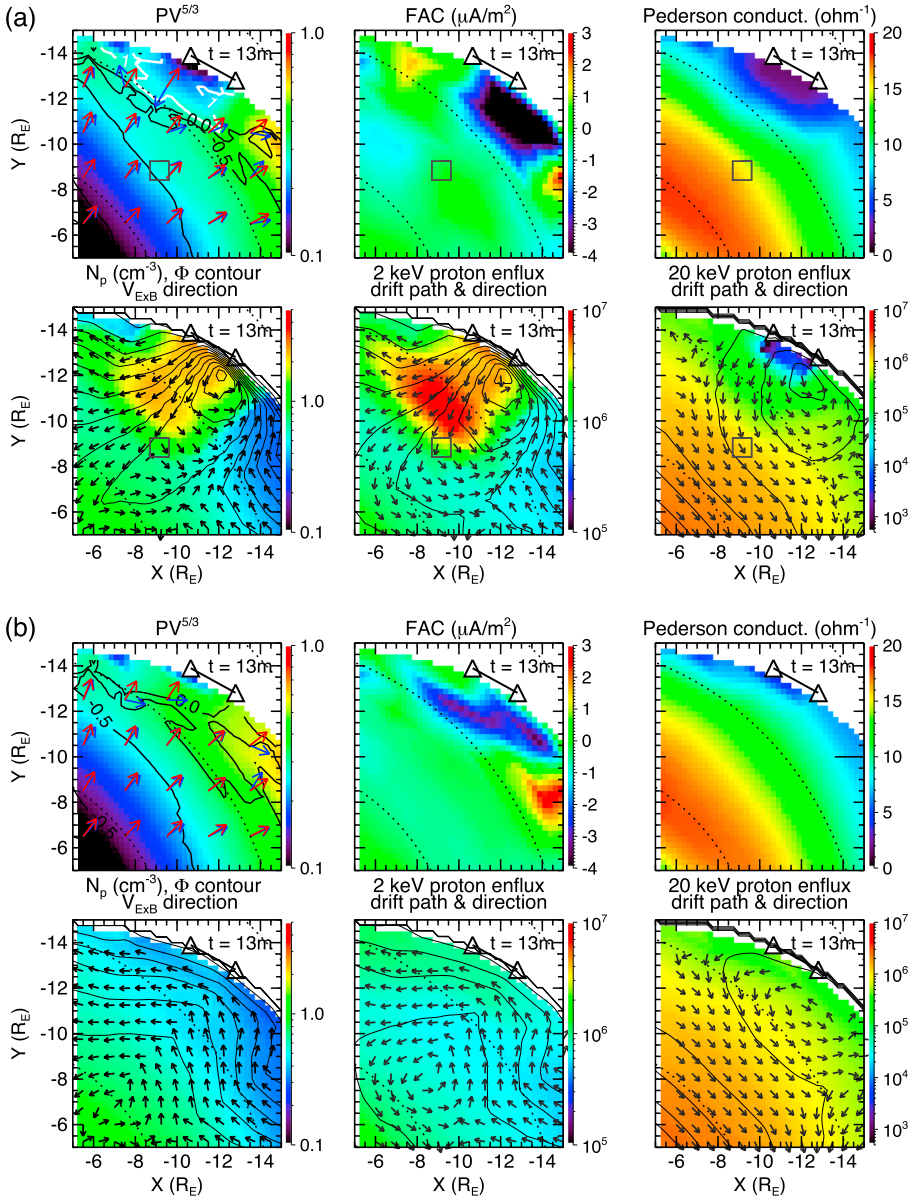

Figure 9. Equatorial distributions of the RCM entropy, ionospheric FACs and Pedersen conductance mapped to the equator, proton density together with electric potential contours (with 4 kV intervals) and electric drift direction, 1 and 20 keV proton energy fluxes (eV/(s sr cm^2 eV)) with drift paths and direction at t = 13 m from (a) Run1 and (b) Run2. In the $PV^{5/3}$ plot, $\nabla PV^{5/3}$ is indicated by the blue vector and ∇V by the red vector. The white contour indicates growth rate = 1, and the black contours indicate growth rate = 0 or −0.5. The two triangles in each plot mark 3 and 3.5 MLT. The squares in Figure 9a indicate the region surrounding dR = 5.5 along the 3 MLT line.

around the newly imposed lower entropy plasma and become weaker radially and azimuthally further away from it. Thus, closer to the 3–3.5 MLT boundary, total drift is more significantly altered by the electric drift perturbation, while further away total drift is more determined by the competition between magnetic drift and the weakened electric drift perturbation. Near the location of dR = 5 R_E along the 3 MLT line (indicated by the squares in Figure 9a), electric drift is small and pointed mainly westward, thus very low-energy protons cannot go further inward. However, at that location particles of higher energy can have their magnetic drift comparable to or higher than electric drift. It can be seen that the total drift of 2 keV protons within the square has larger inward component in comparison to the electric drift, which allows those 2 keV protons to move further inward. This drift difference results in the energy dispersion shown in Figure 8. Therefore, this

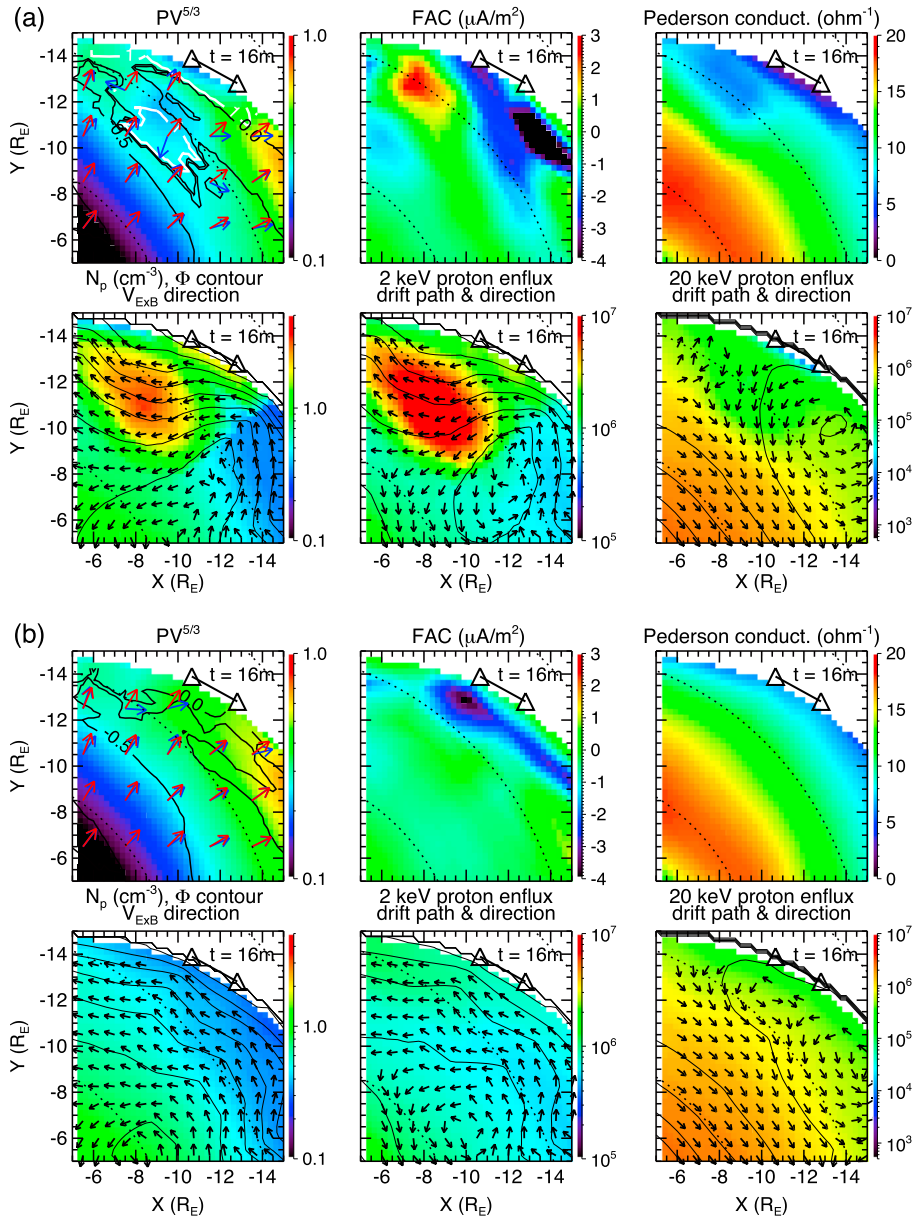

Figure 10. Equatorial distributions of the RCM entropy, ionospheric FACs and Pedersen conductance mapped to the equator, proton density together with electric potential contours (with 4 kV interval) and electric drift direction, 1 and 20 keV proton energy fluxes (eV/(s sr cm^2 eV)) together with drift paths and direction at t = 16 m from (a) Run1 and (b) Run2. In the $PV^{5/3}$ plot, $\nabla PV^{5/3}$ is indicated by the blue vector and ∇V by the red vector. The white contour indicates growth rate = 1, and the black contours indicate growth rate = 0 or −0.5. The two triangles in each plot mark 3 and 3.5 MLT.

competition between electric and magnetic drifts at different locations can likely account for the different energy dispersion signatures observed by different THEMIS probes.

Figure 10a shows the results from Run 1 at t = 16 min when the cold-dense plasma at the boundary is switched off, together with the results of Run2 shown in Figure 10b. As shown in the $PV^{5/3}$ plot, no large entropy gradient perturbation is seen near the 3–3.5 MLT boundary. But there is a region of low entropy ~2 R_E radially away from the boundary associated with the low-entropy plasma that moved inward earlier. This low-entropy plasma is still interchange unstable as indicated by the positive growth rate (the white contour), but its associated electric field perturbations are much smaller than the background large-scale convection electric field as indicated by Run2. The strong radially inward drift seen at t = 13 min is now substantially

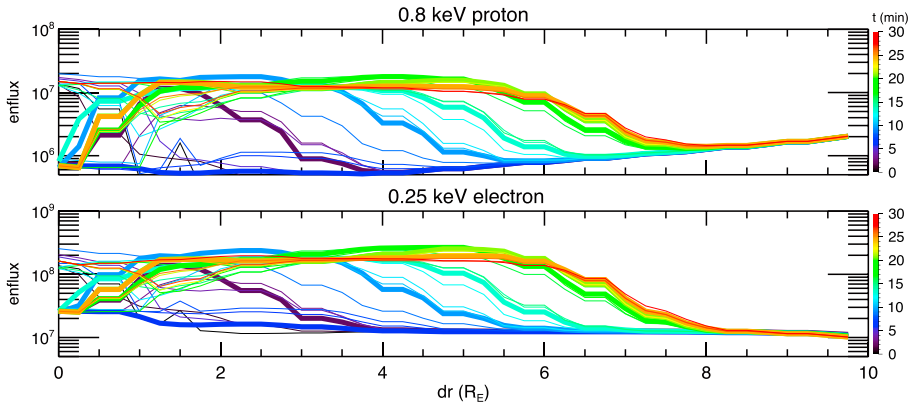

Figure 11. Radial profiles of energy fluxes (eV/(s sr cm^2 eV)) for 0.8 keV proton and 0.25 keV electrons at different times (as indicated by different colors) from Run 1. The thicker lines indicate the times just after the cold-dense boundary is switched off, that is, t = 2, 6, 10, 14, 18, 22, 26, 30 min.

reduced, and the cold-dense plasma drifts mainly toward dawn following the large-scale convection. This continues until the cold-dense plasma boundary condition is switched on again 2 min later, which again creates strong radially inward drift that pushes the cold-dense plasma that came in earlier further inward. This repetitive radial inward pushing by the electric field enhancement caused by the repetitively imposing low-entropy plasma at the boundary allows the cold particles originally at the boundary to gradually move deeper into the magnetosphere. To show more clearly this repetitive inward movement, we plot in Figure 11 the evolution of energy fluxes of low-energy ions and electrons along the 3 MLT line. It can be seen that cold particles further inward each time the K-H boundary condition is switched on. The inward displacement becomes smaller as particle moves deeper into the magnetosphere as a result of smaller electric field perturbations and larger magnetic field.

4. Discussion

The simulation study presented in this paper is the first attempt to investigate whether interchange motion can possibly account for observed appearance of cold-dense ions and electrons. Thus, the specification of the cold-dense plasma boundary condition in the above RCM simulations is rather idealized and simplified so that it is easier to understand the underlying processes. The electric potential at the open-closed field line boundary is likely to change in response to the changes in the cold-dense plasma boundary condition, which was assumed constant in our simulations. In addition, the effect of field-aligned potential drop is not included. We assume that there is only one K-H vortex at the flank with both its width and location fixed in time. In a more realistic condition, there are likely multiple K-H vortices occurring simultaneously at different downtail distances along the flanks as indicated by global simulations of the K-H vortex [e.g., *Claudepierre et al*., 2008; *Li et al*., 2012; *Merkin et al*., 2013]. Since each vortex is only a few R_E wide in the X direction according to the simulations, the vortex observed by TH-B on the nightside is likely different from the one responsible for the cold-dense plasma sheet observed by TH-E, TH-A, and TH-D on the dayside, or it could be the same vortex that is moving tailward. More realistic specification of the cold-dense plasma and electric potential at the boundary based on the simulated K-H vortices should be used in future simulations with the RCM to better understand the time difference in the appearance of cold-dense plasma. More observational study is also needed to compare with the simulation predictions to further evaluate the importance of interchange motion in transporting cold-dense plasma.

Despite the simplified boundary conditions used, our simulations reproduce qualitatively many observed characteristics of cold-dense plasma sheet. There are other predictions from our simulations that may be potentially important but remain to be evaluated in the future. For example, our simulations show local enhancement of FACs associated with the interchange motion, which should have corresponding auroral intensification and ground magnetic field perturbations. Furthermore, the interchange instability associated with the local repetitive low-entropy perturbations at the flank results in flow fluctuations over a much wider region in both MLT and radial distance. Recently, [*Yang et al*., 2014] specified localized and intermittent

entropy perturbations along the tail outer boundary of the RCM-E simulation, which results in intermittent bursty flows on top of large-scale convection flows in the tail plasma sheet. They found that the probability distributions of the simulated flow are consistent with the Geotail observations. Previous observations have shown that the flow fluctuations in both magnitudes and directions with periods of a couple of minutes were seen throughout the plasma sheet during northward IMF, which can lead to inward diffusion of cold-dense plasma in the tail plasma sheet [e.g., *Wang et al*., 2010]. However, it is not expected to have significant entropy perturbations initiated in the tail during northward IMF as assumed in the *Yang et al*. study to drive flow fluctuations. Since the northward IMF is the favorable condition for the K-H instability at the flank magnetopause, it is thus possible that the interchange instability caused by the K-H associated low-entropy plasma drives the flow fluctuations throughout the plasma sheet.

5. Summary

We have presented an event with cold-dense plasma sheet in the near-Earth region observed by all five THEMIS probes at different locations after the IMF turned northward. We found different characteristics in the appearance of cold-dense plasma. TH-B was at the dawn flank magnetopause and periodically saw cold-dense plasma consistent with fluctuations associated with the K-H instability. TH-C, being near the dawn flank, also saw periodically colder and denser plasma with relatively lower entropy. TH-A, TH-D, and TH-E were within the dayside plasma sheet and observed a smoother increase in low-energy particle fluxes, some with energy dispersion. TH-B and TH-C observed large drops in the high-energy particle fluxes when cold-dense plasma appeared while the other three probes observed much smaller drops or no drop. TH-D was only ~1 R_E away from TH-E, but it observed the cold-dense plasma ~20 min later than did TH-E. The changes in the flux tube volume estimated using the Wolf formula suggest that the cold-dense plasma observed by TH-B and TH-C inside the magnetosphere is likely to have relatively lower entropy than the hot plasma sheet plasma.

We specified colder-denser and lower entropy plasma at the RCM outer boundary between 3 and 3.5 MLT periodically with a 2 min period based on the TH-C observation to represent the cold-dense plasma presumably created by the K-H vortices and subsequent reconnection just inside the magnetopause. The perturbation imposed by the lower entropy plasma is interchange unstable and the resulting change in electric field through the M-I coupling gives rise to interchange motion that moves the low-entropy plasma radially inward while replacing it with higher-entropy plasma from the surroundings. This interchange motion transports cold-dense plasma inward from the flanks. It allows the cold-dense plasma sheet to form gradually, and the cold-dense plasma can reach ~7 R_E radially inside the magnetosphere in 30 min. The simulated energy spectrums at different locations are characteristically different in the appearance of cold particles, including fluctuations, mixing with higher-energy particles, and energy dispersion. These different characteristics are qualitatively consistent with those observed by different THEMIS probes, strongly suggesting that the interchange motion is an important transport mechanism in the formation of cold-dense plasma sheet.

Acknowledgments

The work by C.-P. Wang and L.R. Lyons has been supported by NASA grant NNX11AJ12G and NSF grant ATM-1003595. The work by M. Gkioulidou has been supported by NSF grant AGS-1303646. The work by X. Xing has been supported by NASA grant NNX12AD11G. The work by R.A. Wolf has been supported by NASA grant NNX11AJ38G. The THEMIS data are available online (http://artemis.ssl.berkeley.edu/) for free. We thank C.W. Carlson and J.P. McFadden for the use of the ESA data, D. Larson and R.P. Lin for the use of the SST data, and K.H. Glassmeier, U. Auster, and W. Baumjohann for the use of the FGM data. We thank J.H. King, N. Papatashvilli at AdnetSystems, NASA GSFC, and CDAWeb for providing the OMNI data. We thank the support of ISSI International Teams Program: Plasma Entry and Transport in the Plasma Sheet.

Larry Kepko thanks Jay Johnson and Zuyin Pu for their assistance in evaluating this paper.

References

Antonova, E. E. (2006), Quasiturbulent transport and LLBL properties, *Adv. Space Res.*, *37*(3), 532–536.

Borovsky, J. E., and H. O. Funsten (2003), MHD turbulence in the Earth's plasma sheet: Dynamics, dissipation, and driving, *J. Geophys. Res.*, *108*(A7), 1284, doi:10.1029/2002JA009625.

Borovsky, J., R. C. Elphic, H. O. Funsten, and M. F. Thomsen (1997), The Earth's plasma sheet as a laboratory for flow turbulence in high-[beta] MHD, *J. Plasma Phys.*, *57*(1), 1–34.

Chen, C. X., and R. A. Wolf (1993), Interpretation of high-speed flows in the plasma sheet, *J. Geophys. Res.*, *98*, 21,409–21,419, doi:10.1029/93JA02080.

Chen, M. W., and M. Schulz (2001), Simulations of diffuse aurora with plasma sheet electrons in pitch angle diffusion less than everywhere strong, *J. Geophys. Res.*, *106*(A12), 28,949–28,966, doi:10.1029/2001JA000138.

Chen, M. W., C.-P. Wang, M. Schulz, and L. R. Lyons (2007), Solar-wind influence on MLT dependence of plasma sheet conditions and their effects on storm time ring current formation, *Geophys. Res. Lett.*, *34*, L14112, doi:10.1029/2007GL030189.

Claudepierre, S. G., S. R. Elkington, and M. Wiltberger (2008), Solar wind driving of magnetospheric ULF waves: Pulsations driven by velocity shear at the magnetopause, *J. Geophys. Res.*, *113*, A05218, doi:10.1029/2007JA012890.

Echim, M., and J. Lemaire (2002), Positive density gradients at the magnetopause: Interpretation in the framework of the impulsive penetration mechanism, *J. Atmos. Sol. Terr. Phys.*, *64*(18), 2019–2028.

Faganello, M., F. Califano, F. Pegoraro, T. Andreussi, and S. Benkadda (2012), Magnetic reconnection and Kelvin-Helmholtz instabilities at the Earth's magnetopause, *Plasma Phys. Controlled Fusion*, *54*(12), 124,037, doi:10.1088/0741-3335/54/12/124037.

Fairfield, D. H., A. Otto, T. Mukai, S. Kokubun, R. P. Lepping, J. T. Steinberg, A. J. Lazarus, and T. Yamamoto (2000), Geotail observations of the Kelvin-Helmholtz instability at the equatorial magnetotail boundary for parallel northward fields, *J. Geophys. Res.*, *105*, 21,159–21,173, doi:10.1029/1999JA000316.

Fujimoto, M., and T. Terasawa (1994), Anomalous ion mixing within an MHD scale Kelvin-Helmholtz vortex, *J. Geophys. Res.*, *99*(A5), 8601–8613, doi:10.1029/93JA02722.
Fujimoto, M., T. Mukai, and S. Kokubun (2002), Cold-dense plasma sheet and hot-dense ions in the inner-magnetosphere, *Adv. Space Res.*, *30*(10), 2279–2288.
Gkioulidou, M., C.-P. Wang, L. R. Lyons, and R. A. Wolf (2009), Formation of the Harang reversal and its dependence on plasma sheet conditions: RCM simulations, *J. Geophys. Res.*, *114*, A07204, doi:10.1029/2008JA013955.
Gkioulidou, M., C.-P. Wang, and L. R. Lyons (2011), Effect of self-consistent magnetic field on plasma sheet penetration to the inner magnetosphere: RCM simulations combined with modified Dungey force-balanced magnetic field solver, *J. Geophys. Res.*, *116*, A11216, doi:10.1029/2011JA016810.
Gkioulidou, M., C.-P. Wang, S. Wing, L. R. Lyons, R. A. Wolf, and T.-S. Hsu (2012), Effect of an MLT dependent electron loss rate on the magnetosphere-ionosphere coupling, *J. Geophys. Res.*, *117*, A11218, doi:10.1029/2012JA018032.
Harel, M., R. A. Wolf, P. H. Reiff, R. W. Spiro, W. J. Burke, F. J. Rich, and M. Smiddy (1981), Quantitative simulation of a magnetospheric substorm 1, model logic and overview, *J. Geophys. Res.*, *86*, 2217–2241, doi:10.1029/JA086iA04p02217.
Hasegawa, H., M. Fujimoto, K. Takagi, Y. Saito, T. Mukai, and H. Rème (2006), Single-spacecraft detection of rolled-up Kelvin-Helmholtz vortices at the flank magnetopause, *J. Geophys. Res.*, *111*, A09203, doi:10.1029/2006JA011728.
Johnson, J. R., and C. Z. Cheng (1997), Kinetic Alfvén waves and plasma transport at the magnetopause, *Geophys. Res. Lett.*, *24*(11), 1423–1426, doi:10.1029/97GL01333.
Johnson, J. R., and S. Wing (2009), Northward interplanetary magnetic field plasma sheet entropies, *J. Geophys. Res.*, *114*, A00D08, doi:10.1029/2008JA014017.
Lavraud, B., M. F. Thomsen, J. E. Borovsky, M. H. Denton, and T. I. Pulkkinen (2006), Magnetosphere preconditioning under northward IMF: Evidence from the study of coronal mass ejection and corotating interaction region geoeffectiveness, *J. Geophys. Res.*, *111*, A09208, doi:10.1029/2005JA011566.
Li, W., J. Raeder, M. F. Thomsen, and B. Lavraud (2008), Solar wind plasma entry into the magnetosphere under northward IMF conditions, *J. Geophys. Res.*, *113*, A04204, doi:10.1029/2007JA012604.
Li, W. Y., X. C. Guo, and C. Wang (2012), Spatial distribution of Kelvin-Helmholtz instability at low-latitude boundary layer under different solar wind speed conditions, *J. Geophys. Res.*, *117*, A08230, doi:10.1029/2012JA017780.
Liu, S., M. W. Chen, M. Schulz, and L. R. Lyons (2006), Initial simulation results of storm-time ring current in a self- consistent magnetic field model, *J. Geophys. Res.*, *111*, A04225, doi:10.1029/2005JA011194.
Lyon, J. (2011), Numerical simulations of plasma entry, transport, and heating, paper presented at 2011 IUGG General Assembly, Melbourne, Australia.
Ma, X., A. Otto, and P. A. Delamere (2014), Interaction of magnetic reconnection and Kelvin-Helmholtz modes for large magnetic shear: 1. Kelvin-Helmholtz trigger, *J. Geophys. Res. Space Physics*, *119*, 781–797, doi:10.1002/2013JA019224.
McFadden, J. P., C. W. Carlson, D. Larson, V. Angelopoulos, M. Ludlam, R. Abiad, B. Elliott, P. Turin, and M. Marckwordt (2008), The THEMIS ESA plasma instrument and in-flight calibration, *Space Sci. Rev.*, *141*, 277–302, doi:10.1007/s11214-008-9440-2.
Merkin, V. G., J. G. Lyon, and S. G. Claudepierre (2013), Kelvin-Helmholtz instability of the magnetospheric boundary in a three-dimensional global MHD simulation during northward IMF conditions, *J. Geophys. Res. Space Physics*, *118*, 5478–5496, doi:10.1002/jgra.50520.
Nakamura, T. K. M., W. Daughton, H. Karimabadi, and S. Eriksson (2013), Three-dimensional dynamics of vortex-induced reconnection and comparison with THEMIS observations, *J. Geophys. Res. Space Physics*, *118*, 5742–5757, doi:10.1002/jgra.50547.
Nykyri, K., and A. Otto (2001), Plasma transport at the magnetospheric boundary due to reconnection in Kelvin-Helmholtz vortices, *Geophys. Res. Lett.*, *28*(18), 3565–3568, doi:10.1029/2001GL013239.
Otto, A. (2009), Plasma transport and mixing by magnetic reconnection in three-dimensional Kelvin-Helmholtz modes, paper presented at 2009 Plasma Entry and Transport Meeting, Fairbanks, Alaska.
Otto, A., and D. H. Fairfield (2000), Kelvin-Helmholtz instability at the magnetotail boundary: MHD simulation and comparison with Geotail observations, *J. Geophys. Res.*, *105*, 21,175–21,190, doi:10.1029/1999JA000312.
Otto, A., and K. Nykyri (2003), Kelvin-Helmholtz instability and magnetic reconnection: mass transport at the LLBL, in *Earth's Low-Latitude Boundary Layer, Geophys. Monogr. Ser.*, vol. 133, edited by P. T. Newell and T. Onsager, pp. 53–62, AGU, Washington, D. C.
Pontius, D. H., and R. A. Wolf (1990), Transient flux tubes in the terrestrial magnetosphere, *Geophys. Res. Lett.*, *17*(1), 49–52, doi:10.1029/GL017i001p00049.
Robinson, R. M., R. R. Vondrak, K. Miller, T. Dabbs, and D. Hardy (1987), On calculating ionospheric conductances from the flux and energy of precipitating electrons, *J. Geophys. Res.*, *92*, 2565–2569, doi:10.1029/JA092iA03p02565.
Roelof, E. C., and D. G. Sibeck (1993), Magnetopause shape as a bivariate function of interplanetary magnetic field B_z and solar wind dynamic pressure, *J. Geophys. Res.*, *98*(A12), 21,421–21,450, doi:10.1029/93JA02362.
Schulz, M., and M. Chen (2008), Field-line (Euler-potential) model of the ring current, 327, *J. Atmos. Sol. Terr. Phys.*, *70*, 482–489, doi:10.1016/j.jastp.2007.08.063.
Song, P., and C. T. Russell (1992), Model of the formation of the low-latitude boundary layer for strongly northward interplanetary magnetic field, *J. Geophys. Res.*, *97*(A2), 1411–1420, doi:10.1029/91JA02377.
Spence, H. E., and M. G. Kivelson (1993), Contributions of the low-latitude boundary layer to the finite width magnetotail convection model, *J. Geophys. Res.*, *98*(A9), 15,487–15,496, doi:10.1029/93JA01531.
Stepanova, M., V. Pinto, J. A. Valdivia, and E. E. Antonova (2011), Spatial distribution of the eddy diffusion coefficients in the plasma sheet during quiet time and substorms from THEMIS satellite data, *J. Geophys. Res.*, *116*, A00I24, doi:10.1029/2010JA015887.
Takagi, K., C. Hashimoto, H. Hasegawa, M. Fujimoto, and R. TanDokoro (2006), Kelvin-Helmholtz instability in a magnetotail flank-like geometry: Three-dimensional MHD simulations, *J. Geophys. Res.*, *111*, A08202, doi:10.1029/2006JA011631.
Terasawa, T., et al. (1997), Solar wind control of density and temperature in the near-Earth plasma sheet: WIND/GEOTAIL collaboration, *Geophys. Res. Lett.*, *24*(8), 935–938, doi:10.1029/96GL04018.
Thomsen, M. F., J. E. Borovsky, R. M. Skoug, and C. W. Smith (2003), Delivery of cold, dense plasma sheet material into the near-Earth region, *J. Geophys. Res.*, *108*(A4), 1151, doi:10.1029/2002JA009544.
Toffoletto, F., S. Sazykin, R. Spiro, and R. Wolf (2003), Inner magnetospheric modeling with the Rice Convection Model, *Space Sci. Rev.*, *107*, 175–196.
Vasyliunas, V. M. (1970), Mathematical models of magnetospheric convections and its coupling to the ionosphere, in *Particles and Fields in the Magnetosphere*, edited by B. M. McCormac, pp. 60–71, D. Reidel, Hingham, Mass.
Wang, C.-P., L. R. Lyons, M. W. Chen, and F. R. Toffoletto (2004), Modeling the transition of the inner plasma sheet from weak to enhanced convection, *J. Geophys. Res.*, *109*, A12202, doi:10.1029/2004JA010591.

Wang, C.-P., L. R. Lyons, T. Nagai, J. M. Weygand, and R. W. McEntire (2007), Sources, transport, and distributions of plasma sheet ions and electrons and dependences on interplanetary parameters under northward interplanetary magnetic field, *J. Geophys. Res.*, *112*, A10224, doi:10.1029/2007JA012522.

Wang, C.-P., L. R. Lyons, R. A. Wolf, T. Nagai, J. M. Weygand, and A. T. Y. Lui (2009), The plasma sheet $PV^{5/3}$ and nV and associated plasma and energy transport for different convection strengths and AE levels (2009), *J. Geophys. Res.*, *114*, A00D02, doi:10.1029/2008JA013849.

Wang, C.-P., L. R. Lyons, T. Nagai, J. M. Weygand, and A. T. Y. Lui (2010), Evolution of plasma sheet particle content under different interplanetary magnetic field conditions, *J. Geophys. Res.*, *115*, A06210, doi:10.1029/2009JA015028.

Wang, C.-P., M. Gkioulidou, L. R. Lyons, R. A. Wolf, V. Angelopoulos, T. Nagai, J. M. Weygand, and A. T. Y. Lui (2011), Spatial distributions of ions and electrons from the plasma sheet to the inner magnetosphere: comparisons between THEMIS-Geotail statistical results and the Rice Convection Model, *J. Geophys. Res.*, *116*, A11216, doi:10.1029/2011JA016809.

Weygand, J. M., et al. (2005), Plasma sheet turbulence observed by Cluster II, *J. Geophys. Res.*, *110*, A01205, doi:10.1029/2004JA010581.

Wing, S., J. R. Johnson, P. T. Newell, and C.-I. Meng (2005), Dawn-dusk asymmetries, ion spectra, and sources in the northward interplanetary magnetic field plasma sheet, *J. Geophys. Res.*, *110*, A08205, doi:10.1029/2005JA011086.

Wolf, R. A. (1983), The quasi–static (slow–flow) region of the magnetosphere, in *Solar Terrestrial Physics*, edited by R. L. Carovillano and J. M. Forbes, pp. 303–368, D. Reidel, Hingham, MA.

Wolf, R. A., V. Kumar, F. R. Toffoletto, G. M. Erickson, A. M. Savoie, C. X. Chen, and C. L. Lemon (2006), Estimating local plasma sheet $PV^{5/3}$ from single-spacecraft measurements, *J. Geophys. Res.*, *111*, A12218, doi:10.1029/2006JA012010.

Xing, X. (2008), *Criterion for Interchange Instability in the Plasma Sheet*, Rice Univ., Houston, Tex.

Xing, X., and R. A. Wolf (2007), Criterion for interchange instability in a plasma connected to a conducting ionosphere, *J. Geophys. Res.*, *112*, A12209, doi:10.1029/2007JA012535.

Yang, J., F. R. Toffoletto, R. A. Wolf, and S. Sazykin (2011), RCM-E simulation of ion acceleration during an idealized plasma sheet bubble injection, *J. Geophys. Res.*, *116*, A05207, doi:10.1029/2010JA016346.

Yang, J., F. R. Toffoletto, R. A. Wolf, S. Sazykin, P. A. Ontiveros, and J. M. Weygand (2012), Large-scale current systems and ground magnetic disturbance during deep substorm injections, *J. Geophys. Res.*, *117*, A04223, doi:10.1029/2011JA017415.

Yang, J., R. A. Wolf, F. R. Toffoletto, S. Sazykin, and C.-P. Wang (2014), RCM-E simulation of bimodal transport in the plasma sheet, *Geophys. Res. Lett.*, *41*, 1817–1822, doi:10.1002/2014GL059400.